Journal of the Mechanics and Physics of Solids 61 (2013) 2015–2033

Contents lists available at SciVerse ScienceDirect

Journal of the Mechanics and Physics of Solids

journal homepage: www.elsevier.com/locate/jmps

Oliver–Pharr indentation method in determining elastic moduli of shape memory alloys—A phase transformable material

Qianhua Kan [a], Wenyi Yan [b,*], Guozheng Kang [a], Qingping Sun [c]

[a] School of Mechanics and Engineering, Southwest Jiaotong University, 610031 Chengdu, China
[b] Department of Mechanical & Aerospace Engineering, Monash University, Clayton, VIC 3800, Australia
[c] Department of Mechanical Engineering, The Hong Kong University of Science and Technology, Clear Water Bay, Kowloon, Hong Kong, China

ARTICLE INFO

Article history:
Received 8 October 2012
Received in revised form
24 March 2013
Accepted 25 May 2013
Available online 10 June 2013

Keywords:
Oliver–Pharr method
Spherical indentation
Elastic modulus
Shape memory alloys
Phase transformation

ABSTRACT

Instrumented indentation test has been extensively applied to study the mechanical properties such as elastic modulus of different materials. The Oliver–Pharr method to measure the elastic modulus from an indentation test was originally developed for single phase materials. During a spherical indentation test on shape memory alloys (SMAs), both austenite and martensite phases exist and evolve in the specimen due to stress-induced phase transformation. The question, "What is the measured indentation modulus by using the Oliver–Pharr method from a spherical indentation test on SMAs?" is answered in this paper. The finite element method, combined with dimensional analysis, was applied to simulate a series of spherical indentation tests on SMAs. Our numerical results indicate that the measured indentation modulus strongly depends on the elastic moduli of the two phases, the indentation depth, the forward transformation stress, the transformation hardening coefficient and the maximum transformation strain. Furthermore, a method based on theoretical analysis and numerical simulation was established to determine the elastic moduli of austenite and martensite by using the spherical indentation test and the Oliver–Pharr method. Our numerical experiments confirmed that the proposed method can be applied in practice with satisfactory accuracy. The research approach and findings can also be applied to the indentation of other types of phase transformable materials.

1. Introduction

Instrumented indentation techniques have been widely applied to characterize the mechanical behavior of elasto-plastic materials at small scale (Nix and Gao, 1998; Hay and Pharr, 2000; Oliver and Pharr, 2004; Cheng and Cheng, 2004). More recently, indentation tests have been extended to study the mechanical properties of multi-phase functional materials (Ni et al., 2002, 2003; Yan et al., 2006a, 2006b, 2007; Qian et al., 2006; Feng et al., 2008, etc.) and biological materials (Zysset et al., 1999; Ebenstein and Pruitt, 2006; Oyen and Cook, 2009; Ishimoto et al., 2011, etc.).

Shape memory alloys, represented by NiTi, are well known smart materials due to their unique super-elastic and shape memory properties, and have found many engineering applications such as actuators, biomedical devices and implants

* Corresponding author. Tel.: +61 3 99020113; fax: +61 3 99051825.
E-mail address: wenyi.yan@monash.edu (W. Yan).

0022-5096/$ - see front matter
http://dx.doi.org/10.1016/j.jmps.2013.05.007

Table 1
Summary of austenite elastic modulus E_a and martensite elastic modulus E_m reported in literature.

E_a (GPa)	E_m (GPa)	E_m/E_a	Reference
70	45	0.64	Zaki and Moumni (2007)
72	45	0.63	Kang et al. (2009)
61.2	27.6	0.45	Wang and Yue (2007)
70	30	0.43	Popov and Lagoudas (2007)
67	26.3	0.39	Dye (1990)
47	17	0.36	Auricchio (1995)
31	20	0.65	Sun and Li (2002), Li and Sun (2002)
33	21	0.64	Feng and Sun (2006)
43	22	0.51	Qian et al. (2006)

(see Duerig et al., 1999; Humbeeck, 1999; Fu et al., 2004). There is a growing interest in probing the micro- and nano-scale mechanical properties of SMAs using indentation techniques since these alloys are also used as thin films and micro-devices in micro-electro-mechanical systems (Gall et al., 2001; Ni et al., 2002; Qian et al., 2004; Zhang et al., 2006; Amini et al., 2011). The micro- or nano-indentation response of SMAs is more complicated than that of single phase materials because transformation occurs between two phases, austenite and martensite, during indentation loading and unloading. There is a remarkable difference in the elastic moduli of the austenite and martensite phases. Experimental results published in literature, summarized in Table 1, show that the ratio of the martensite elastic modulus to that of the austenite varies from 0.36 to 0.65.

The Oliver–Pharr method (Oliver and Pharr, 1992) is the most frequently adopted method in instrumented indentation testing to probe the elastic modulus of materials. However, this method was originally developed and therefore is valid only for single-phase materials. When applied to SMAs where two phases of different moduli coexist during indentation, the question, "What does the measured indentation modulus mean?" arises. The answer to this question will not only advance our understanding of the indentation response of SMAs or other phase transformable materials, but may also lead to a new way of characterizing the elastic modulus of the martensite phase and/or the austenite phase at very small scales. These two issues form the objectives of the present study.

The structure of this paper is as follows. The isothermal constitutive model of SMAs is briefly described in Section 2.1. In Section 2.2, a theoretical analysis of the spherical indentation modulus of SMAs obtained from the Oliver–Pharr method is presented. A numerical model is described in Section 3.1 and applied in Section 3.2 to examine the indentation modulus and to identify the contribution of individual phases and indentation depth on the indentation modulus. In Section 3.3, a weighting factor is introduced and numerically examined to develop the relationship between the indentation modulus and the elastic moduli of the austenite and the martensite phases and the indentation depth. Following the results of Section 3.3, a spherical indentation method to predict elastic moduli of both austenite and martensite of SMAs is presented in Section 3.4. Section 3.5 describes a set of numerical experiments performed to validate the proposed method. Conclusions are given in Section 4.

2. Theoretical analysis

2.1. Constitutive model of SMAs

The super-elastic behavior and shape memory effect of SMAs can be illustrated by stress–strain curves under a uniaxial loading–unloading cycle. Idealized tensile stress–strain curves from a super-elastic SMA and an SMA with the shape memory effect are shown in Fig. 1(a) and (b), respectively.

Super-elastic behavior can be observed during the loading and unloading process above the austenite finish temperature and is associated with the stress-induced martensite transformation and the reverse transformation during unloading (Fig. 1(a)). Different from a super-elastic SMA, reverse transformation does not happen in the unloading process below the austenite start temperature for an SMA with the shape memory effect, and the residual strain can only be recovered by increasing the temperature to above the austenite finish temperature (Fig. 1(b)). As shown in Fig. 1(a) and (b), σ_f^s and σ_f^e are the start and end stresses for the forward transformation, respectively; σ_r^s and σ_r^e are the start and end stresses for the reverse transformation, respectively; linear transformation hardening is considered by setting $\sigma_f^e > \sigma_f^s$. E_a and E_m are the elastic moduli of the austenite and the martensite, respectively; ε_m is the maximum transformation strain. Additionally, v_a and v_m are the elastic Poisson's ratios of austenite and martensite, respectively. ε_v is the transformation volume strain.

A phenomenological 3D constitutive model (Auricchio et al., 1997; Auricchio and Taylor, 1997) describing the macroscopic super-elastic and shape memory effect of SMAs has been verified and implemented into Abaqus (2010). The implemented model is based on general inelastic frame, the total strain $\boldsymbol{\varepsilon}$ can be decomposed into elastic strain $\boldsymbol{\varepsilon}^e$ and

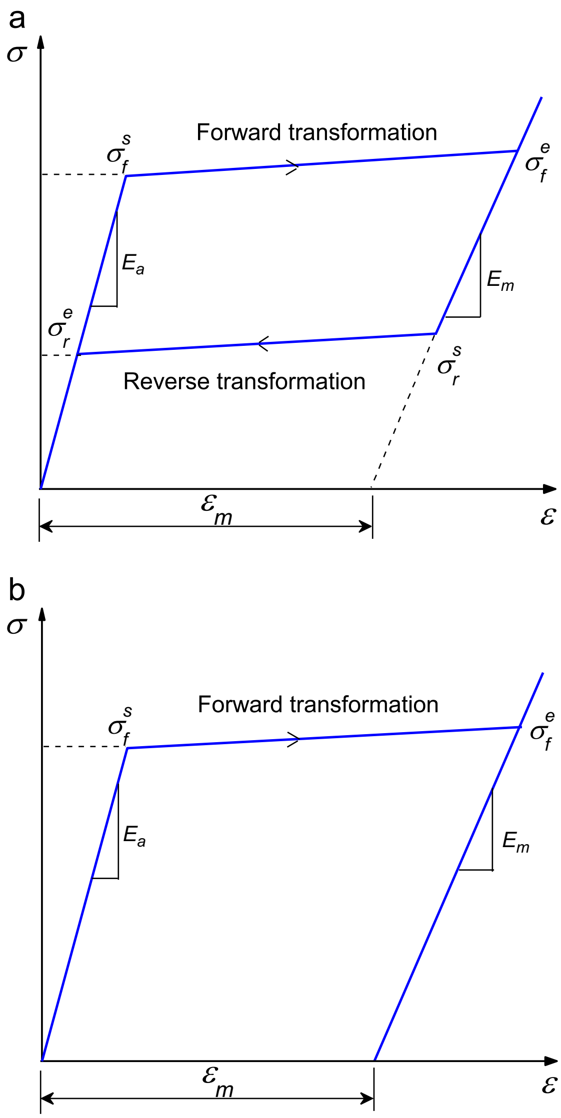

Fig. 1. Idealized stress–strain curves of SMAs under uniaxial loading: (a) super-elasticity, including forward transformation and reverse transformation with transformation hardening; (b) shape memory effect, only forward transformation occurs, the residual strain can be recovered by increasing the temperature.

transformation strain $\boldsymbol{\varepsilon}^{tr}$, i.e.,

$$\boldsymbol{\varepsilon} = \boldsymbol{\varepsilon}^{e} + \boldsymbol{\varepsilon}^{tr} \tag{1}$$

The plastic deformation of the martensite under a high stress level (e.g., 1600 MPa, see Qian et al., 2006) is neglected in the implemented model. Therefore, the deformation response in our current study is limited to elasticity and phase transformation under the indentation of a spherical indenter.

The elastic strain is assumed to be related to the stress by the effective elastic modulus tensor $\mathbf{D}_{am}(z)$:

$$\boldsymbol{\sigma} = \mathbf{D}_{am}(z) : \boldsymbol{\varepsilon}^{e} = \mathbf{D}_{am} : (\boldsymbol{\varepsilon} - \boldsymbol{\varepsilon}^{tr}) \tag{2}$$

where z is the martensite volume fraction. The effective modulus $\mathbf{D}_{am}(z)$ is obtained from the Reuss scheme (Auricchio and Sacco, 1997a, 1997b)

$$\frac{1}{\mathbf{D}_{am}} = \left(\frac{1}{\mathbf{D}_{a}}(1-z) + \frac{1}{\mathbf{D}_{m}} z \right) \tag{3}$$

where $\mathbf{D}_A$ and $\mathbf{D}_M$ are the austenite and martensite elastic modulus tensors, respectively. The expression for the effective modulus $\mathbf{D}_{am}$ allows a description of the elastic modulus of a mixture of the austenite and martensite phases.

The model is constructed from the basic assumption that the martensitic transformation mechanism is associated to an active reorientation process, described by the following equation:

$$\boldsymbol{\varepsilon}^{tr} = \varepsilon_m z \frac{\partial F(\boldsymbol{\sigma}, T)}{\partial \boldsymbol{\sigma}} \tag{4}$$

where $F(\boldsymbol{\sigma}, T)$ is a stress $\boldsymbol{\sigma}$ and temperature T dependent loading function, which drives the martensitic transformation process. To model a different material response between traction and compression, Drucker–Prager type loading functions are introduced for the forward and the reverse transformation:

$$F(\boldsymbol{\sigma}, T) = ||\mathbf{s}|| + 3\alpha p - C_a T \tag{5a}$$

$$F(\boldsymbol{\sigma}, T) = ||\mathbf{s}|| + 3\alpha p - C_m T \tag{5b}$$

where $\mathbf{s} = \boldsymbol{\sigma} - p\mathbf{I}$ is the deviatoric stress tensor and $p = \frac{1}{3}\boldsymbol{\sigma} : \mathbf{I}$ is the hydrostatic pressure, $\mathbf{I}$ is the second rank unit tensor. Parameter α reflects the anisotropic transformation responses in tension and compression. The quantities C_a and C_m are the Clausius–Clapeyron constants for the forward and the reverse transformation, respectively.

It should be noted that the implemented model can predict uniaxial behavior of NiTi SMA very well since the material parameters of the model are mainly obtained from uniaxial tests (Auricchio et al., 1997; Auricchio and Taylor, 1997). The model has also been validated by simulating three-point and four-point bending tests, the biaxial non-proportional loading of a flat sheet and the Luders-band effect (Auricchio et al., 1997). In the present study, the loading at a material point due to indentation is three-dimensional and non-proportional. Our investigation indicates that this Abaqus built-in material model for SMAs has the capacity to predict not only the uniaxial and but also the nonproportionally multiaxial response of NiTi SMA. Details of the study are presented in Appendix A.

2.2. Indentation modulus of an SMA from Oliver–Pharr method

The Oliver–Pharr method (Oliver and Pharr, 1992) was originally developed to measure the hardness and elastic modulus of a single phase elasto-plastic material from the indentation load–depth curve with sharp indenters, such as a pyramidal Berkovich tip. It has been proven that this method can also be applied in any axisymmetrical indenter geometries including a sphere (Oliver and Pharr, 2004).

The Oliver–Pharr method begins by fitting the unloading portion of the indentation load–depth data to the power-law relation shown below:

$$P = \alpha (h - h_f)^m \tag{6}$$

where α and m are the fitting parameters. Originally, h_f has the physical meaning of the final depth after complete unloading. Practically, when the Oliver–Pharr method is applied, h_f becomes a fitting parameter and only the upper unloading data are used to fit Eq. (6) through regression analysis (Oliver and Pharr, 1992, 2004).

As shown in Fig. 2, our numerical results confirm that the power law Eq. (6) can also be applied to well fit the upper unloading curve of a spherical indentation curve from an SMA either with shape memory effect (Fig. 2(a)) or with super-elasticity (Fig. 2(b)), although the deformation mechanism is different for these two types of SMAs. Only elastic deformation of the austenite and the martensite, transformed from the indentation loading, occurs during unloading for SMAs with shape memory effect, while the entire unloading process of the super-elastic SMA consists of three stages: elastic unloading of a mixture of austenite and martensite, reverse transformation and pure austenite elastic unloading. P_m and h_m, displayed in Fig. 2, are the maximum indentation load and the maximum indentation depth, respectively. It is worth commenting that the fitted h_f is close to the residual indentation depth, its original physical meaning, for SMA (Fig. 2a) with shape memory effect, which is similar to elasto-plastic materials, while the fitted h_f has lost this physical meaning and become a purely fitting parameter for super-elastic SMA (Fig. 2b).

Once the three fitting parameters α, m and h_f in Eq. (6) are obtained, the contact stiffness S, which is defined as the slope of the unloading curve at the maximum indentation depth, can be computed from

$$S = \frac{dP}{dh}\Big|_{h = h_m} = Bm(h_m - h_f')^{m-1} \tag{7}$$

The contact depth of the spherical indentation h_c can be calculated by following the Oliver–Pharr method as

$$h_c = h_m - 0.75\frac{P_m}{S} \tag{8}$$

"Pile-up" ($h_c/h_m > 1$) and "sink-in" ($h_c/h_m < 1$) phenomena are usually observed in ordinary elasto-plastic materials, and the degree of "pile-up" and "sink-in" depends on the plastic yield stress and the level of strain-hardening (Giannakopoulos and Suresh, 1999). Eq. (8) is only suitable for "sink-in" due to the positive indentation load P_m and contact stiffness S. Numerical studies show that "pile-up" does not occur in SMAs with a high martensite plastic yield stress over 1300 MPa (Kang and Yan, 2010). As mentioned above, plasticity is excluded in this study, i.e., the martensite plastic yield stress can be treated as infinite. Therefore, Eq. (8) can be used to obtain the contact depth in all the cases studied in this paper. The

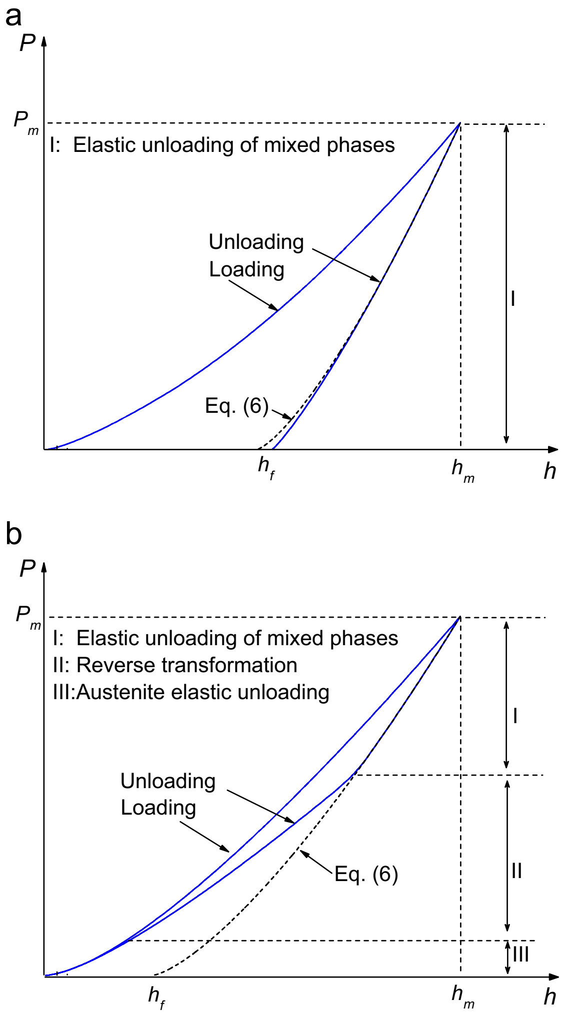

Fig. 2. Typical spherical indentation load–depth curve (obtained from FE simulations) with the upper unloading curve fitted by Eq. (6) for (a) an SMA with shape memory effect and the unloading process consisting of elastic unloading of mixed austenite and martensite phases; (b) a super-elastic SMA with the unloading process consisting of three stages: the elastic unloading of a mixture of austenite and martensite phases, reverse transformation and austenite elastic unloading.

contact area A_c can be computed directly from the contact depth h_c and the radius of the indenter tip R

$$A_c = \pi(2Rh_c - h_c^2) \tag{9}$$

The contact stiffness S from Eq. (7) and the contact area A_c from Eq. (9) are used to calculate the reduced modulus

$$E_r = \frac{\sqrt{\pi}}{2\beta}\frac{S}{\sqrt{A_c}} \tag{10}$$

where β is a dimensionless correction factor which accounts for the deviation in stiffness due to the lack of axisymmetry of the indenter tip with $\beta = 1.0$ for axisymmetric indenters, $\beta = 1.012$ for a square-based Vickers indenter, and $\beta = 1.034$ for a triangular Berkovich punch (King, 1987). For spherical indentations, β is taken as unity in this work.

After obtaining the reduced modulus E_r from Eq. (10), the indentation modulus from the Oliver–Pharr method can be finally determined by

$$E_{op} = \frac{1-v_s^2}{(1/E_r)-((1-v_i^2)/E_i)} \tag{11a}$$

where v_s is Poisson's ratio of the specimen, E_i and v_i are respectively the elastic modulus and Poisson's ratio of the indenter. For ordinary single phase materials, the indentation modulus obtained from Eq. (11a) is the elastic modulus of the specimen. If the indenter's elastic modulus E_i is much larger than that of the specimen (e.g., SMAs), the indenter can be treated as a rigid body and Eq. (11a) can be simplified as

$$E_{op} = (1-\nu_s^2)E_r \tag{11b}$$

In a spherical indentation test on a SMA with the assumption of a rigid indenter, the indentation modulus E_{op} depends on SMA's material properties E_a, E_m, σ_f^s, σ_f^e, σ_r^s, σ_r^e, ε_m, ε_v, ν_s, as well as the maximum indentation depth h_m, the indenter tip radius R and the friction coefficient μ, i.e.,

$$E_{op} = f_1(E_a, E_m, \sigma_f^s, \sigma_f^e, \sigma_r^s, \sigma_r^e, \nu_a, \nu_m, \varepsilon_m, \varepsilon_v, h_m, R, \mu) \tag{12a}$$

Different from the elastic indentation of non-homogeneous material systems such as a thin film-substrate system, where the two phases are fixed and analytical methods can be applied (Gao et al., 1992), indentation of SMAs with the evolving of the two phase volumes is very complex and numerical methods are required to obtain the indentation response in a theoretical study. Recently, the finite element method was successfully applied to study the mechanics of indentation of plastically graded materials (Choi et al., 2008). The finite element method was applied here to simulate the spherical indentation on SMAs. The finite element model is discussed in Section 3.1.

Our numerical results indicate that the reverse transformation during indentation unloading for a super-elastic SMA has a negligible influence on the indentation modulus. For example, the change of the normalized reverse stress σ_r^s/E_a from 0.001 to 0.004 only results in the difference of less than 1.2% in the indentation modulus. Consequently, σ_r^s and σ_r^e, the start and end stress for the reverse transformation, can be removed from Eq. (12a). More importantly, it indicates that all the results presented afterwards can be applied to both super-elastic SMAs and the SMAs with shape memory effect.

Assuming a linear transformation hardening, the hardening coefficient η can be formulated as $\eta = (\sigma_f^e - \sigma_f^s)/(\varepsilon_m E_a)$. Poisson's ratio $\nu_s(=\nu_a=\nu_m)$ of SMAs is generally set as a constant. The transformation volume strain ε_v for NiTi SMAs is around −0.39% (Holtz et al., 1999; Jacobus et al., 1996), which is much smaller than the transformation shear strain components ($\sim$5%). It was found that its influence on the load–depth curve can be neglected (Yan et al., 2008). Our numerical investigation concludes that the influence of the transformation volume strain on indentation modulus is negligibly small ($<$0.57%). Additionally, the friction coefficient has a negligible influence on the indentation modulus. For example, our numerical results show that the maximum difference in indentation modulus is less than 1.6% if the friction varies from 0 to 0.3. Thus a frictionless assumption is made between the indenter and the sample. Based on these considerations, Eq. (12a) can be further simplified as

$$E_{op} = f_2(E_a, E_m, \sigma_f^s, \eta, \varepsilon_m, h_m, R) \tag{12b}$$

According to dimensional analysis (Cheng and Cheng, 1999, 2004), the dimensionless indentation modulus E_{op}/E_a can be expressed as

$$\frac{E_{op}}{E_a} = \prod\nolimits_1 \left(\frac{E_m}{E_a}, \frac{\sigma_f^s}{E_a}, \eta, \varepsilon_m, \frac{h_m}{R} \right) \tag{13}$$

Eq. (13) clearly indicates that the indentation modulus depends on not only the mechanical properties of the two phases but also the indentation depth. It is evident that when the indentation depth is very small, i.e., $h_m/R \to 0$, the specimen is of a single austenite phase and $E_{op}/E_a = 1$. With the increase in the indentation depth, phase transformation from austenite to martensite occurs and the transformation zone increases gradually. As a result, the normalized indentation modulus E_{op}/E_a varies with the normalized indentation depth h_m/R. Eventually, E_{op}/E_a will approach E_m/E_a. How indentation depth h_m/R affects indentation modulus E_{op}/E_a in SMAs with different material properties is examined numerically by the finite element method in the following section.

3. Numerical investigation

3.1. Finite element model

The commercial finite element package Abaqus (2010) was applied to perform the numerical simulations. Considering that the indenter tip is normally made of diamond, which has a much higher elastic modulus than those of SMAs, a rigid spherical indenter is used in the numerical analysis. As shown in Fig. 3(a), the spherical indentation was modeled as a 2D axisymmetric problem using a total of 8157 four-node linear axisymmetric elements (CAX4). Roller boundary condition is imposed on the symmetric axis of the sample and the bottom is constrained in both the radial and axial directions, the size of the sample is 30 times larger than the radius of the indenter to avoid the influence of the boundaries introduced in the numerical model (see Fig. 3(a)). A refined mesh is used in the area beneath the indenter tip and load P is applied in the reference point as illustrated in Fig. 3(b).

A preliminary mesh sensitivity analysis was performed to ensure that the mesh is fine enough such that the simulated results are insensitive to the element size in the indenter tip region. The minimum element size near the contact surface was finally determined as 0.15% of the indenter radius. Because the contact stiffness is calculated from the slope of the unloading curve, the elastic modulus obtained from the Oliver–Pharr method is only related to the unloading process at the initial stage. To accurately obtain the unloading data by using Abaqus, 2000 increments were employed for a single unloading

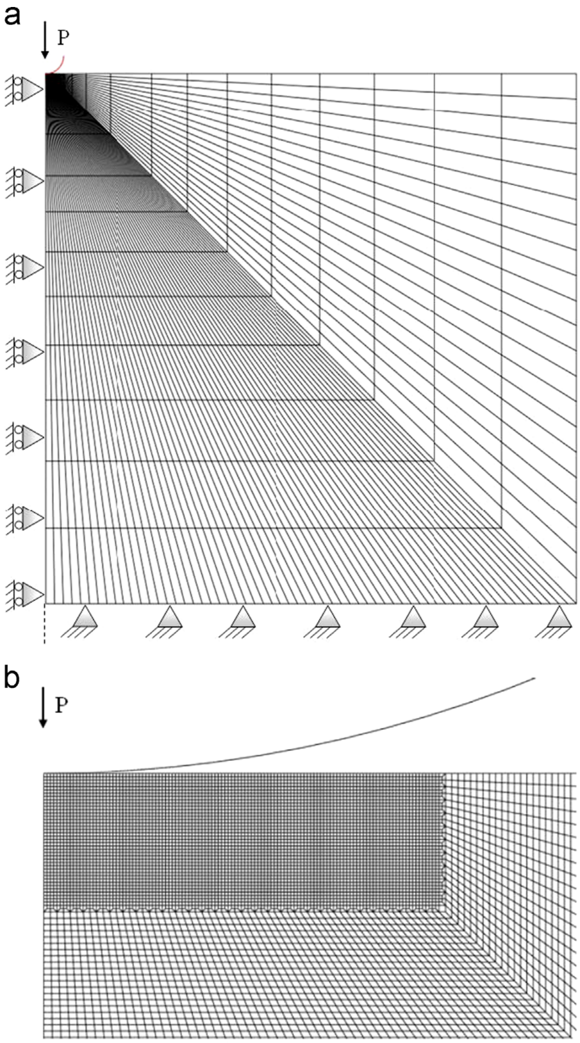

Fig. 3. Finite element model for the indentation tests with a spherical indenter: (a) the entire model and (b) the fine mesh near the indenter tip.

simulation. In all the simulations, Poisson's ratios v_a and v_m were fixed at 0.3, which is reasonable for SMAs. The austenite elastic modulus was set as a constant ($E_a = 100$ GPa). To obtain an accurate indentation modulus E_{op} in computational simulations, a key factor is to accurately calculate the contact stiffness S. Readers are referred to the Appendix B for details on this issue.

3.2. Numerical results of indentation modulus E_{op}

Referring to Eq. (13), the effect of the ratio E_m/E_a on the indentation modulus E_{op}/E_a is firstly examined. Fig. 4 shows the relationship between the indentation modulus E_{op}/E_a obtained from the Oliver–Pharr method and the maximum indentation depth h_m/R with different ratios of E_m/E_a from 0.4 to 0.7, where the maximum transformation strain ε_m, the forward transformation stress σ_f^s/E_a and the transformation hardening coefficient η are set as 0.08, 0.005 and 0.0, respectively. It can be seen clearly that when the maximum indentation depth is very small (e.g., $h_m/R \leq 0.001$), the indentation modulus E_{op}/E_a remains almost a constant at unity, which means that the indentation modulus is the same as that of the austenite due to the fact that phase transformation has not occurred yet and the sample is in the austenite phase. With the further increase of h_m/R, E_{op}/E_a decreases. As the transformed martensite zone increases with the indentation depth, E_{op}/E_a is approaching the lower bound value of E_m/E_a (Dashed lines and arrowheads show the corresponding relations between E_{op}/E_a and E_m/E_a in Fig. 4.) It is worth noting that the martensite elastic modulus E_m cannot be simply obtained at a very large indentation depth. The first reason is that the sample will never become a single martensite phase material, no matter how large the indentation depth is. The second reason is that the Oliver–Pharr method cannot provide

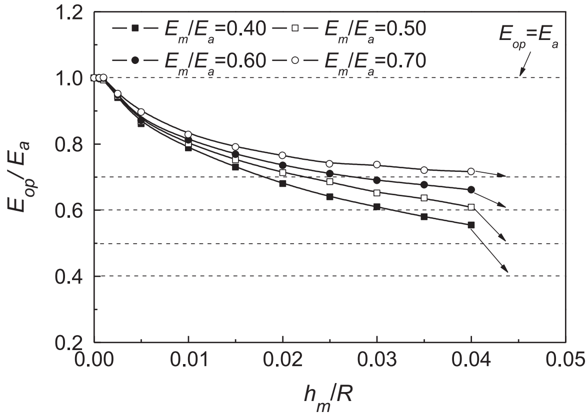

Fig. 4. Relationship between the normalized indentation modulus E_{op}/E_a and the normalized maximum indentation depth h_m/R with different ratios of E_m/E_a ($\sigma_f^s/E_a = 0.005$, $\varepsilon_m = 0.08$, $\eta = 0.0$).

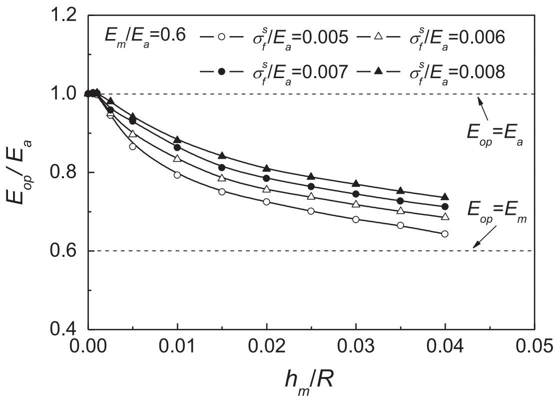

Fig. 5. Relationship between the normalized indentation modulus E_{op}/E_a and the normalized maximum indentation depth h_m/R with different values of the normalized forward transformation stress σ_f^s/E_a ($E_m/E_a = 0.6$, $\varepsilon_m = 0.06$, $\eta = 0.0$).

enough accuracy at very large ratios of h_m/R (see Fig. B1 in Appendix B). Additionally, Fig. 4 indicates that for a given indentation depth, E_{op}/E_a increases with E_m/E_a.

The effect of σ_f^s/E_a on E_{op}/E_a versus h_m/R relationship is shown in Fig. 5, where σ_f^s/E_a varies from 0.005 to 0.008, which is the practical range for most SMA materials. In all the cases, the values of E_m/E_a, ε_m and η are fixed as constants ($E_m/E_a = 0.6$, $\varepsilon_m = 0.06$ and $\eta = 0.0$). The calculated results in Fig. 5 show that the indentation modulus E_{op}/E_a decreases from 1.0 to approaching 0.6 due to a fixed E_m/E_a of 0.6. This confirms further that when the maximum indentation depth is very small (e.g., $h_m/R \le 0.001$), the indentation modulus E_{op}/E_a remains almost a constant at unity, while it decreases with h_m/R. As shown in Fig. 5, for a given maximum indentation depth h_m/R, E_{op}/E_a increases with an increase in σ_f^s/E_a due to the decrease in the volume of transformed martensite.

The effect of the transformation hardening coefficient η on E_{op}/E_a is shown in Fig. 6, where η varies from 0.0 to 0.1, while E_m/E_a, σ_f^s/E_a and ε_m are taken as constant values of 0.6, 0.005, and 0.06, respectively. Similarly, when $h_m/R \le 0.001$, $E_{op}/E_a = 1.0$. With the increase in h_m/R, E_{op}/E_a decreases. It is seen that the transformation hardening coefficient η also has influence on the indentation modulus E_{op}/E_a, which cannot be neglected when h_m/R is larger than 0.01.

The effect of ε_m on E_{op}/E_a is shown in Fig. 7, where ε_m ranges from 4% to 10%, while E_m/E_a, σ_f^s/E_a and η are fixed as 0.6, 0.005 and 0.0, respectively. The dependency of E_{op}/E_a on h_m/R is confirmed again in all the cases shown in Fig. 7: E_{op}/E_a is around unity at very small h_m/R ratios (e.g., $h_m/R \le 0.001$) and decreases with h_m/R. It is seen that compared with other parameters, ε_m has a relatively small effect on E_{op}/E_a. For a given h_m/R, E_{op}/E_a increases slightly with ε_m.

Based on all the numerical results presented in Figs. 4–7, it can be concluded that the indentation modulus E_{op} obtained from a spherical indentation test of SMAs by using the Oliver–Pharr method is neither the elastic modulus of the martensite nor the elastic modulus of the austenite. E_{op}/E_a depends on the indentation depth h_m/R as well as other material parameters (E_m/E_a, σ_f^s/E_a, η and ε_m). A semi-empirical relationship between E_{op}, E_a and E_m will be established by introducing a weighting factor in the next section.

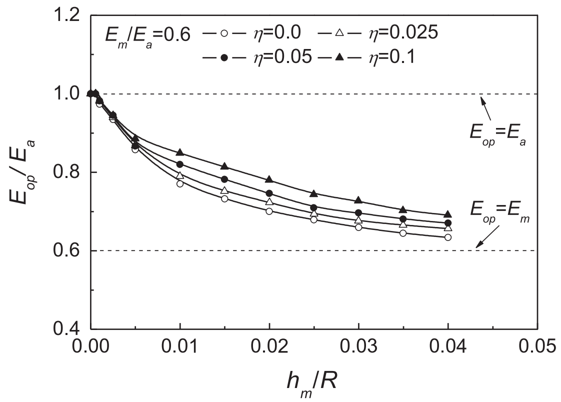

Fig. 6. Relationship between the normalized indentation modulus E_{op}/E_a and the normalized maximum indentation depth h_m/R with different values of the transformation hardening coefficient η (E_m/E_a = 0.6, σ_f^s/E_a = 0.005, ε_m = 0.06).

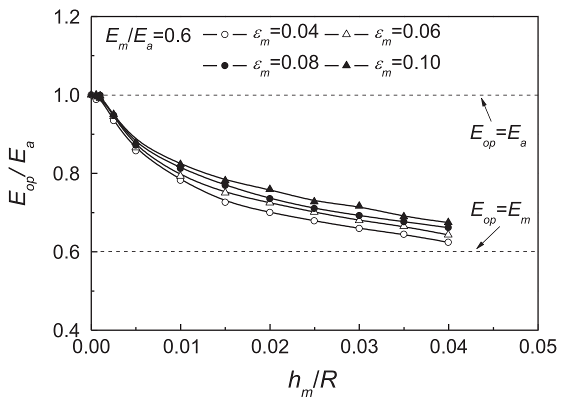

Fig. 7. Relationship between the normalized indentation modulus E_{op}/E_a obtained from the Oliver–Pharr method and the normalized maximum indentation depth h_m/R with different values of the maximum transformation strain ε_m(E_m/E_a = 0.6, σ_f^s/E_a = 0.005, η = 0.0).

3.3. Weighting factor θ

The austenite and martensite phase zones in the specimen beneath the indenter tip can be identified by the distribution of the martensite volume fraction, z, obtained from a finite element simulation, as shown in Fig. 8 for a typical SMA. It is noted that the martensite volume fraction z is calculated at every integration point. It only depends on the material model and the loading including loading history at the point. It is seen that the material evolves in three stages with the increase in the indention depth: a single austenite phase at the initial stage (Fig. 8(a)), a partial transformation zone (A–M) at the second stage, which is surrounded by the austenite phase (Fig. 8(b)) and a fully transformed martensite zone at the final stage, which is surrounded by a partially transformed zone enclosed by the austenite phase (Fig. 8(c)).

Due to the three-stage phase evolution during a spherical indention test, the indentation specimen should be considered as a non-homogeneous material and the level of the non-homogeneity varies with the indentation depth. To develop a relationship between the indentation modulus E_{op} and the elastic modulus E_a and E_m of the two phases, a weighting factor θ which characterizes the effect of the martensite phase is introduced. It is noted that the sample is in a pure austenite phase when indentation depth is very small, and we have $E_{op} = E_a$. In contrast, the contact zone is dominated by the martensite phase at a very large indentation depth, therefore, we expect $E_{op} \to E_m$. So, the weighting factor θ must satisfy the conditions: $E_{op} = E_a$ when $\theta = 0$ and $E_{op} \to E_m$ if $\theta \to 1$. One option is to choose θ by following the form of the Reuss scheme in dealing with composite materials, which is expressed as

$$\frac{1}{E_{op}} = \frac{1}{E_a}(1-\theta) + \frac{1}{E_m}\theta \tag{14}$$

The weighting factor θ in Eq. (14) represents the effect of the transformed martensite phase on the measured indentation modulus from the Oliver–Pharr method. It is worth commenting that the weighting factor θ is different from the martensite

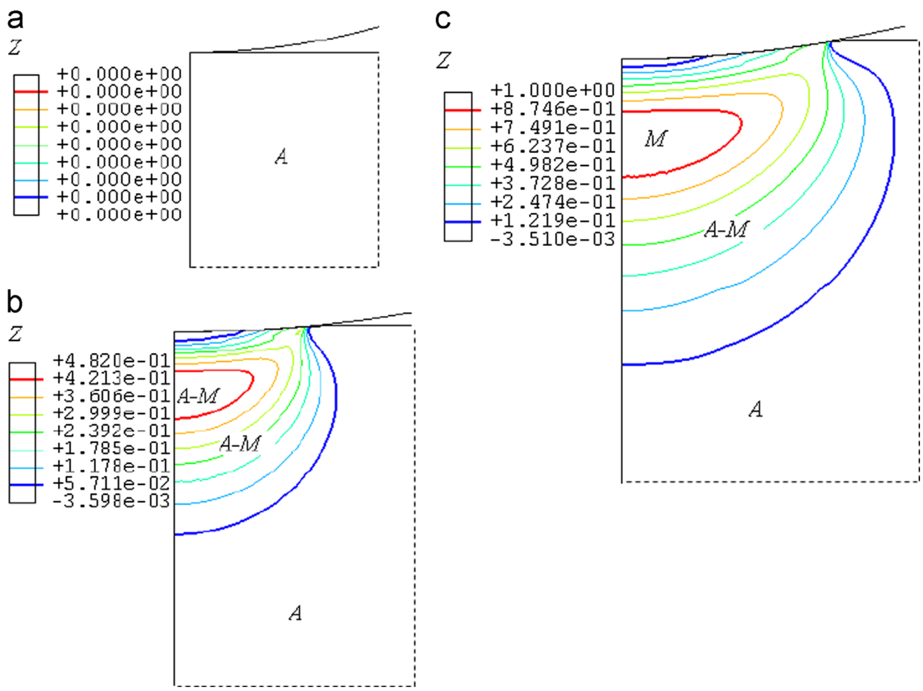

Fig. 8. Evolution of the material phases during a typical spherical indentation test with three stages, represented by the distribution of the martensite volume fraction z: (a) single austenite phase (A); (b) mixed austenite and martensite zone (A–M) enclosed by pure austenite phase and (c) pure martensite zone (M), mixed phase zone (A–M) and pure austenite phase zone (A).

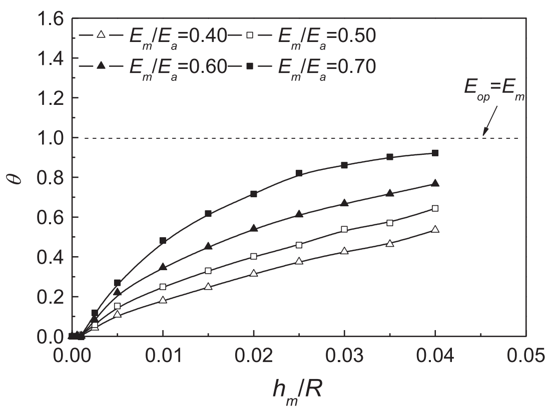

Fig. 9. Relationship between the weighting factor θ and the normalized maximum indentation depth h_m/R with different ratios of E_m/E_a ($\sigma_f^s/E_a = 0.005$, $\varepsilon_m = 0.08$, $\eta = 0.0$).

volume fraction z in Eq. (3). The weighting factor θ is always smaller than one, i.e., $0 \le \theta < 1$, as the indentation specimen will never become a single martensite phase material while the martensite volume fraction z at any point can vary from zero to one, i.e., $0 \le z \le 1$.

According to Eqs. (12b) and (14), the dimensionless weighting factor θ is a function of the ratio E_m/E_a, the normalized forward transformation stress σ_f^s/E_a, the transformation hardening coefficient η, the maximum transformation strain ε_m and the normalized maximum indentation depth h_m/R, i.e.,

$$\theta = \Pi_2\left(\frac{E_m}{E_a}, \frac{\sigma_f^s}{E_a}, \eta, \frac{h_m}{R}\right) \tag{15}$$

Similar to the study of E_{op} in the previous section, the relationship Eq. (15) can be examined numerically, as shown in Figs. 9–12. It can be concluded from the numerical results that the modulus ratio E_m/E_a, forward transformation stress σ_f^s/E_a,

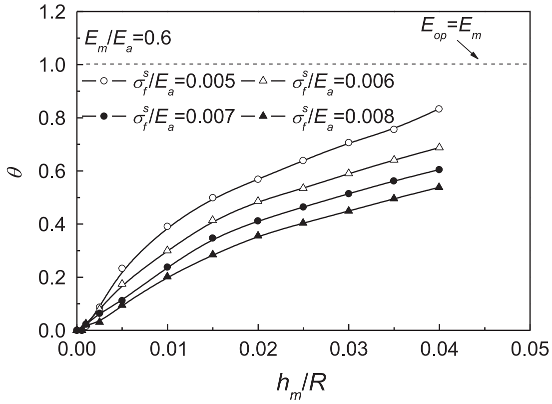

Fig. 10. Relationship between the weighting factor θ and the normalized maximum indentation depth h_m/R with different values of the normalized forward transformation stress σ_f^s/E_a ($E_m/E_a = 0.6$, $\varepsilon_m = 0.06$, $\eta = 0.0$).

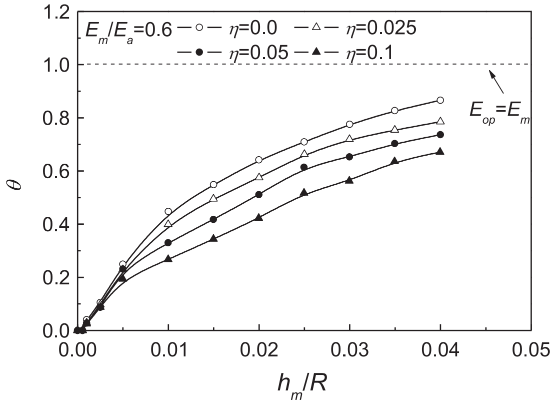

Fig. 11. Relationship between the weighting factor θ and the normalized maximum indentation depth h_m/R with different values of the transformation hardening coefficient η ($E_m/E_a = 0.6$, $\sigma_f^s/E_a = 0.005$, $\varepsilon_m = 0.06$).

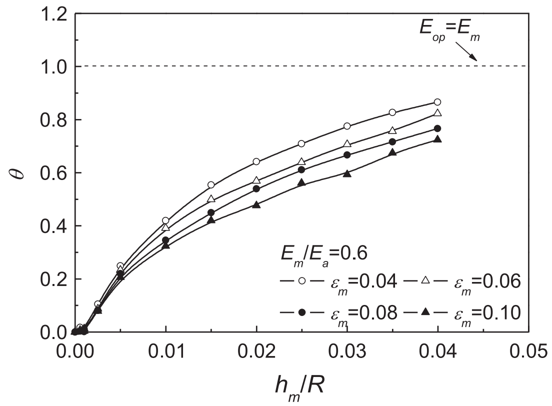

Fig. 12. Relationship between the weighting factor θ and the normalized maximum indentation depth h_m/R with different values of the maximum transformation strainε_m ($E_m/E_a = 0.6$, $\sigma_f^s/E_a = 0.005$, $\eta = 0.0$).

transformation hardening coefficient η, maximum transformation strain ε_m and the maximum indentation depth have significant influence on the weighting factor θ. In all the simulated cases, it can be observed that the weighting factor θ is zero at very small h_m/R ratios (e.g., $h_m/R \le 0.001$) due to single phase elastic contact and it subsequently increases exponentially with h_m/R. Based on the numerical results, a semi-empirical formula is proposed to quantify the relationship between θ and h_m/R as follows:

$$\theta = 1 - e^{-\gamma(\langle h_m - h_0\rangle/R)} \tag{16}$$

where h_0 is the critical indentation depth for the commencing of the phase transformation during an indentation loading test. $\langle x\rangle$ is McCauley's bracket and it means: $\langle x\rangle = 0$ for $x \le 0$, and $\langle x\rangle = x$ for $x > 0$. The parameter γ controls the evolution of the weighting factor θ and it depends on material properties E_a, E_m, σ_f^s, ε^{tr} and η. It can be seen from Eq. (12) that when h_m is smaller than h_0, the value of θ equals 0.0. The specimen is a single phase material with pure austenite. With the increase in h_m/R, the specimen consists of two phases due to stress induced martensitic transformation and θ increases exponentially with h_m due to the martensite phase zone increase, which describes well the numerical results in Figs. 9–12.

Eq. (16) has in fact separated the influence of the maximum indentation depth h_m/R on the indentation results from the other material parameters. Such a treatment provides a basis to establish a semi-empirical method with a simple experimental procedure to determine E_a and E_m, which are discussed in the following subsection.

3.4. Indentation method to predict E_a and E_m

Substituting Eq. (16) into Eq. (14), we obtain

$$\frac{1}{E_{op}} = \frac{1}{E_a} e^{-\gamma(\langle h_m - h_0\rangle/R)} + \frac{1}{E_m}\left(1 - e^{-\gamma(\langle h_m - h_0\rangle/R)}\right) \tag{17}$$

The semi-empirical formula Eq. (17) explicitly relates E_{op} from the Oliver–Pharr method with h_m. Consequently, a spherical indentation method to measure the elastic moduli of SMAs can be proposed and it is described below.

First, the elastic modulus of the austenite E_a and the critical elastic indentation depth h_0 can be determined based on previous studies. According to Hertzian elastic contact theory, the elastic indentation load before forward phase transformation is determined by (Hertz, 1896)

$$P = \frac{4}{3(1-\nu_a^2)} R^{1/2} h^{3/2} E_a \tag{18}$$

The austenite elastic modulus E_a can be directly calculated from the load–depth curve by Eq. (18). Our numerical results show that the austenite elastic modulus E_a obtained from Eq. (18) has a maximum error of 1.99% when the maximum indentation depth h_m/R is less than 0.001. Additionally, the elastic limit load P_0 at the onset of phase transformation is related to the forward transformation stress σ_f^s through (Yan et al., 2006a)

$$\frac{P_0}{E_a R} = 17.92\left(\frac{\sigma_f^s}{E_a}\right)^3 \tag{19}$$

Eq. (19) can be directly used to determine the forward transformation stress σ_f^s in theory. Practically, it is difficult to identify the elastic limit load P_0 because the transition from pure elastic deformation to martensitic transformation is very smooth and is not an abrupt change in the load–displacement curve. Yan et al. (2006a) shown the accuracy of locating the transition point, and therefore, the accuracy of determining the forward transformation stress σ_f^s, can be significantly improved by using the indentation slope curve instead of the indentation curve. Furthermore, they found the accuracy of the predicted σ_f^s depends on the transformation hardening behavior. If the hardening is small or zero, the accuracy can be very high.

Combining Eqs. (18) and (19), the critical elastic indentation depth of austenite h_0 can be obtained

$$\frac{h_0}{R} = 5.31\left(\frac{\sigma_f^s}{E_a}\right)^2 \tag{20}$$

To validate Eq. (20), a finite element simulation was carried out and the material parameters chosen were $E_a = 50$ GPa and $\sigma_f^s = 500$ MPa. The radius of indenter R was 100 μm. The value of h_0 from FE simulation has only a difference of 0.9% from the one obtained by Eq. (20) (52.6 nm versus 53.1 nm).

After determining E_a and h_0 from the stage of elastic spherical indentation, there are only two unknown parameters E_m and γ left in Eq. (17) and they can be determined mathematically from a set of E_{op} versus h_m/R data with different indentation depths by regression analysis.

Detailed steps for predicting the elastic moduli of both austenite and martensite of SMAs by the Oliver–Pharr method are summarized as follows:

(1) A set of indentation tests with different indentation depths is firstly carried out.
(2) The austenite elastic modulus E_a can be obtained from the Oliver–Pharr method or directly from Eq. (18) at a small indentation depth (e.g., $h_m/R \le 0.001$), and the forward transformation stress σ_f^s can be determined according to Eq. (19) from the spherical indentation test. Then, the critical elastic depth of austenite h_0 can be obtained by Eq. (20).
(3) The relationship between elastic modulus E_{op} and the ratio $(h_m - h_0)/R$ can be obtained from load–depth curves with different indentation depths by using the Oliver–Pharr method.

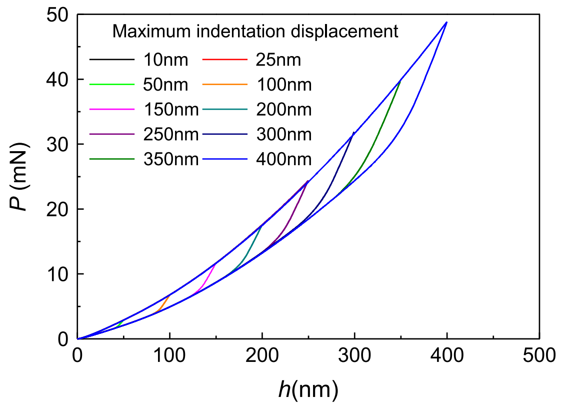

Fig. 13. Load–depth curves at different maximum indentation depths of an SMA with $E_m/E_a=0.7$, $\sigma_f^s=500$ MPa, $\eta=0.0$ and $\varepsilon_m=0.04$.

(4) The martensite elastic modulus E_m and the parameter γ can be determined from a set of $1/E_{op}$ vs. $(h_m-h_0)/R$ data by employing regression analysis according to Eq. (17).

3.5. Numerical experiments

In order to validate the proposed method to predict the elastic moduli of both austenite and martensite, a set of numerical experiments have been performed. As an example, Fig. 13 shows the load–depth curves of a super-elastic SMA simulated under repeated loading–unloading at different maximum indentation depths from 10 nm to 400 nm. The values of the material parameters used in the finite element simulations were chosen as $E_m/E_a=0.7$, $\sigma_f^s=500$ MPa, $\sigma_r^s=300$ MPa, $\eta=0.0$, and $\varepsilon_m=0.04$, the radius of indenter R was 10 μm. The value of austenite elastic modulus was fixed as 100 GPa. It can be observed that well-defined hysteresis loops are produced during each loading and unloading cycle. Such hysteresis loops are due to the intrinsic super-elasticity of this material.

A set of simulations with reasonable values of material parameters for different SMAs were carried out. The elastic moduli of both austenite and martensite can be obtained by the steps described in Section 3.4. Table 2 provides a comparison between the input elastic modulus in the FEM simulations and the predicted elastic modulus from the indentation curves. It is found that the predicted moduli are good agreement with the input moduli. It is known that the stability of the solution is very important and has been discussed in similar inverse problems of indentation (Cao and Lu, 2005; Zhao et al., 2006; Buljak and Maier, 2012). In the present study, the errors are caused by three aspects: the first is the error in obtaining indentation curves by FE simulations; the second is the error in calculating indentation modulus by using the Oliver–Pharr method, and the last is the fitting error by Eq. (17). The errors can be evaluated by comparing the predicted elastic moduli of both austenite and martensite phases with those input ones:

$$Error=\frac{|E_{input}-E_{prediction}|}{E_{input}} \tag{21}$$

It is shown that the maximum error for the prediction of the austenite elastic modulus is only 1.99% and 12.62% for martensite, which would be satisfactory in real indentation tests of SMAs. Very large or very small ratios of the elastic modulus E_m/E_a result in large errors (e.g., 12.19%, 9% for $E_m/E_a=0.8$, 0.4, respectively, (see Table 2)). A high forward transformation stress (e.g., $\sigma_f^s>600$ MPa) also causes a large error (11%, 12.62% for $\sigma_f^s=700$, 900 MPa, respectively). In other cases, the error for the martensite elastic modulus E_m is less than 6.2%.

It is noted that the error sensitivity analysis discussed above corresponds to the idealized numerical problem, that is, a numerical experiment of a spherical indentation. In practice, the non-idealized indenter tip and the smoothness of the experimental curves will impose some additive errors on the proposed method, which needs the real indentation experiments to validate the proposed method.

4. Conclusions

Theoretical analysis and finite element simulation were performed to investigate the measured indentation modulus by applying the Oliver–Pharr method in a spherical indentation test on SMAs. The effects of the elastic modulus of the transformed martensite, the indentation depth, the forward transformation stress, the maximum transformation strain and the transformation hardening coefficient on the measured indentation modulus were discussed. Our numerical results clearly indicate that the indentation modulus is neither the elastic modulus of the martensite nor the elastic modulus of the

Table 2
Comparison between input elastic moduli in FE simulations and predicted elastic moduli by the proposed method (E_a = 100 GPa and σ_r^s = 300 MPa as input values in all cases).

Input parameters in Abaqus							E_a (GPa)	Error (%)	E_m (GPa)	Error (%)
E_m (GPa)	σ_f^s (MPa)	σ_r^s (MPa)	η	ε_m	ε_v	μ				
40	500	300	0.0	0.08	0.0	0.0	99.57	0.43	43.60	9.00
50	500	300	0.0	0.08	0.0	0.0	99.35	0.65	54.10	8.20
60	500	300	0.0	0.08	0.0	0.0	99.76	0.24	62.52	4.20
70	500	300	0.0	0.08	0.0	0.0	100.12	0.12	70.32	0.46
60	500	300	0.0	0.04	0.0	0.0	99.85	0.15	61.56	2.60
70	500	300	0.0	0.04	0.0	0.0	99.52	0.48	66.19	5.44
80	500	300	0.0	0.04	0.0	0.0	99.31	0.69	70.25	12.19
60	500	300	0.0	0.06	0.0	0.0	98.99	1.01	62.32	3.87
60	600	300	0.0	0.06	0.0	0.0	98.36	1.64	63.53	5.88
60	700	300	0.0	0.06	0.0	0.0	98.49	1.51	66.60	11.00
60	900	300	0.0	0.06	0.0	0.0	98.62	1.38	67.57	12.62
60	600	400	0.0	0.06	0.004	0.0	99.44	0.56	64.45	7.53
60	600	300	0.0	0.06	0.004	0.0	99.45	0.55	65.73	9.29
60	600	200	0.0	0.06	0.004	0.0	99.44	0.56	65.57	8.65
60	600	100	0.0	0.06	0.004	0.0	100.82	0.82	65.02	8.36
60	500	300	0.025	0.04	0.0	0.0	98.12	1.88	63.72	6.20
60	500	300	0.05	0.04	0.0	0.0	98.20	1.80	63.68	6.13
60	500	300	0.1	0.04	0.0	0.0	98.34	1.66	62.50	4.17
60	500	300	0.0	0.08	0.0	0.0	99.92	0.08	63.67	6.12
60	500	300	0.0	0.10	0.0	0.0	99.19	0.81	62.06	3.43
60	500	300	0.0	0.06	0.002	0.0	98.01	1.99	62.89	4.82
60	500	300	0.0	0.06	0.004	0.0	98.12	1.88	62.50	4.17
60	500	300	0.0	0.06	0.0	0.1	98.62	1.38	62.50	4.17
60	500	300	0.0	0.06	0.0	0.2	98.46	1.54	62.11	3.52
60	500	300	0.0	0.06	0.0	0.3	98.81	1.19	61.73	2.88

austenite and that in particular strongly depends on the indentation depth among all other parameters. At a very small indentation depth (e.g., $h_m/R \leq 0.001$), before the commencing of phase transformation, the specimen is a single phase material and the Oliver–Pharr method can be applied directly. The measured indentation modulus is indeed the elastic modulus of the austenite. Once phase transformation occurs, the measured indentation modulus decreases with the indentation depth due to the increase in the volume of the transformed martensite.

Additionally, a weighting factor, which represents the contribution of the transformed martensite, was introduced to establish a relationship between the measured indentation modulus from the Oliver–Pharr method and the elastic moduli of both the austenite and martensite phase. A semi-empirical formula was then proposed to quantify the weighting factor based on our numerical results, which leads to an explicit relationship between the measured indentation modulus and the elastic moduli of the austenite, the martensite and the indentation depth. Finally, a spherical indentation test method by using this established explicit relationship and the Oliver–Pharr method was proposed to measure the elastic moduli of the austenite and martensite of SMAs. This proposed indentation method was validated by a set of 25 numerical experiments. The numerical results show the maximum errors were only 1.99% for austenite elastic modulus and 12.62% for martensite elastic modulus, which would be acceptable in practice. This research outcome has the potential in extending the application of the Oliver–Pharr method from single phase materials to phase transformation materials.

Acknowledgments

This work was financially supported by the National Natural Science Foundation of China (11025210 and 11202171) and the Fundamental Research Funds for the Central Universities of China (SWJTU12CX044). This research was carried out during Qianhua Kan's academic visit to Monash University with financial support from the Australian Government's Endeavour Awards program under the scheme of Endeavour Research Fellowships. The authors are grateful to the two unknown reviewers for their helpful comments for improving the manuscript.

Appendix A. Validation of the implemented model

A NiTi SMA tube under uniaxial and non-proportional multiaxial loadings was simulated by using the implemented model in Abaqus at 300 K. The predicted results are compared with experimental tests. NiTi tubes (Ni, 55.9 at%) with

Table A1
Material parameters used in simulations.

E_a=40.8 GPa, E_m=24.2 GPa, ν_a=0.3, ν_m=0.3, ε_m=0.0447, ε_ν=0.0
σ_f^s=390 MPa, σ_f^e=479 MPa, σ_r^s=106 MPa, σ_r^e=50 MPa
T_0=296 K, C_a=6.04 MPa/K, C_m=7.79 MPa/K

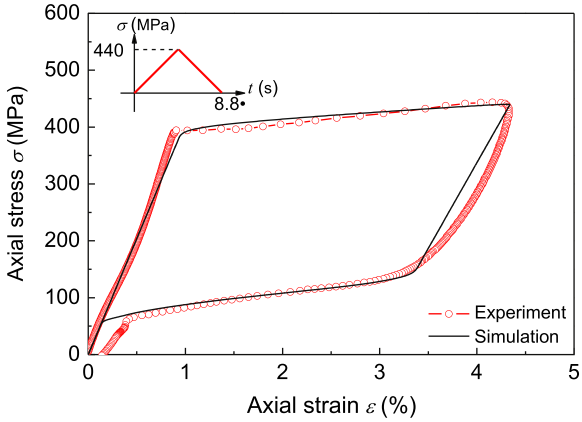

Fig. A1. Superelastic behavior under tension loading–unloading..

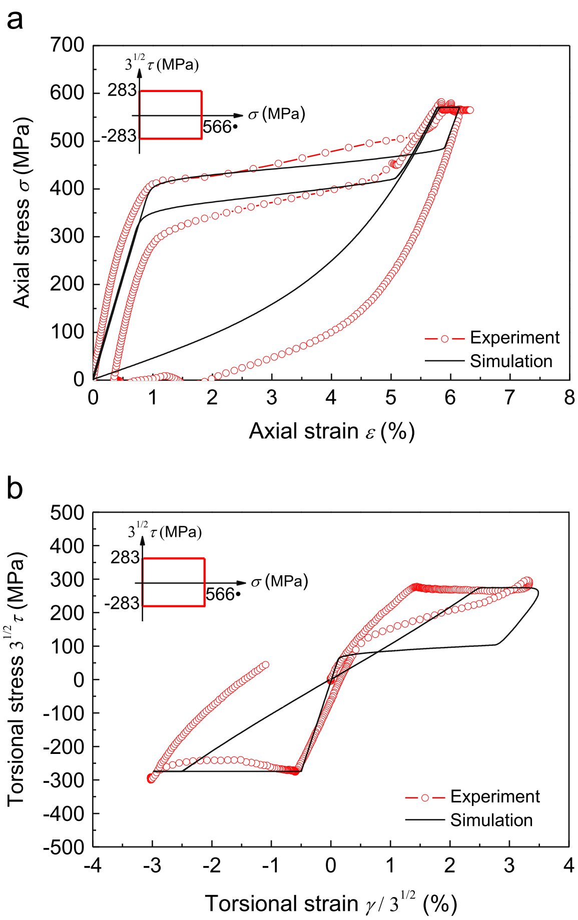

Fig. A2. Comparison between predictions by Abaqus and experimental data under non-proportional multiaxial tension–torsional rectangle path: (a) axial strain–axial stress response and (b) torsional strain–torsional stress response.

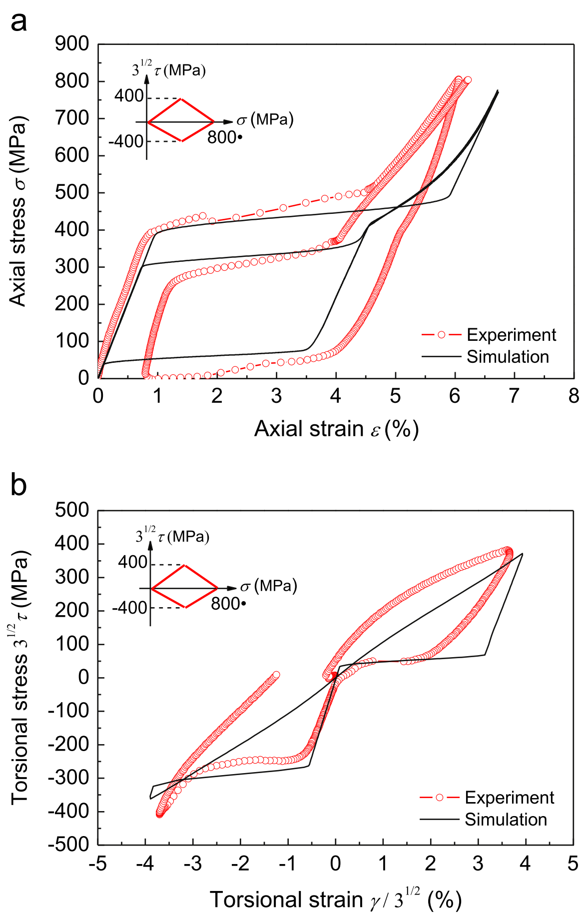

Fig. A3. Comparison between predictions by Abaqus and experimental data under non-proportionally multiaxial tension–torsional rhombus path: (a) axial strain–axial stress response and (b) torsional strain–torsional stress response.

$A_f = 290$ K were employed in the experimental tests. The tubular specimen has the outer diameter of 2.01 mm and inner diameter of 1.68 mm. Material parameters are obtained from a uniaxial tension-unloading curve and listed in Table A1.

Fig. A1 shows the experimental and simulated uniaxial stress–strain curves. It is seen that the model can predict uniaxial deformation behavior very well.

To investigate the performance of the material model in predicting non-proportionally multiaxial loading conditions, the simulations and experiments under rectangle, rhombus and hourglass stress-driven tension–torsion paths were performed, as shown in Figs. A2–A4. It is seen that the experimental observed deformation behavior of the NiTi SMA under these nonproportionally multiaxial loadings can be reproduced by the implemented model. Some difference between experimental and simulation result is caused by the residual strain occurs in the unloading process due to plastic deformation, which is neglected by the material model.

Appendix B. Indentation unloading curve fitting in applying the Oliver–Pharr method

When the Oliver–Pharr method is applied in measuring elastic modulus and hardness of elasto-plastic solid materials, Hay and Pharr (2000) suggested using 25–50% of the upper indentation unloading data for curve fitting so as to achieve a satisfactory prediction accuracy. In the case of SMAs, this rule of thumb may not be applicable due to the reverse phase transformation during unloading. The issue of how much unloading data should be applied in the indentation of SMAs is addressed in this appendix through analyzing the numerical results.

The FE model is described in Section 3.1. The values of material parameters were chosen as $E_a = E_m = 50$ GPa, $\varepsilon_m = 0.04$, $\sigma_f^s = \sigma_f^e = 500$ MPa and $\sigma_r^s = \sigma_r^e = 300$ MPa. Note that the elastic moduli of the austenite and the martensite are intentionally taken as the same for the current investigation. The errors between the elastic modulus E_{op} obtained from the Oliver–Pharr method and the elastic modulus E_a as input value in FE simulations can be quantified as $(|E_a - E_{op}|/E_a) \times 100\%$. The

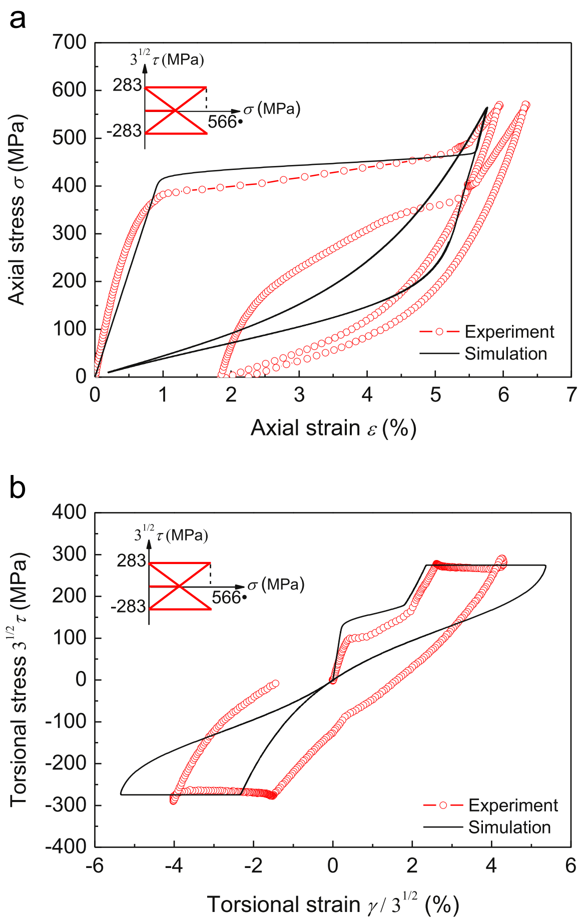

Fig. A4. Comparison between predictions by Abaqus and experimental data under non-proportional multiaxial tension–torsional hourglass path: (a) axial strain–axial stress response and (b) torsional strain–torsional stress response.

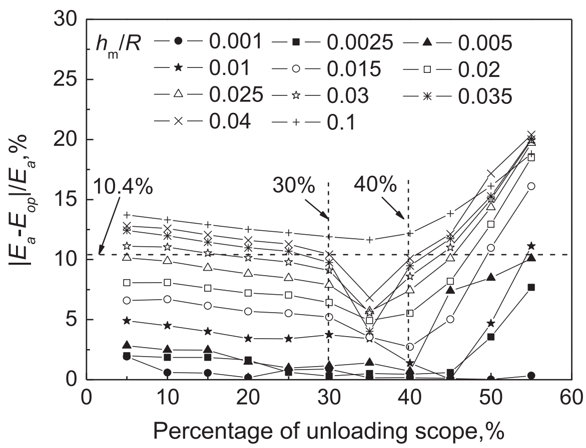

Fig. B1. Error of the predicted elastic modulus by the Oliver–Pharr method as a function of the percentage of the upper unloading data used in the prediction under different indentation depths.

normalized indentation depth h_m/R varies from 0.001 to 0.1 and the percentage of the upper unloading data used in the prediction varies from 5% to 55% in the following numerical investigation.

Fig. B1 shows the relationship between the error and the percentage of the upper unloading data used in the prediction at different normalized indentation depths h_m/R. It can be seen that when the value of h_m/R is relatively

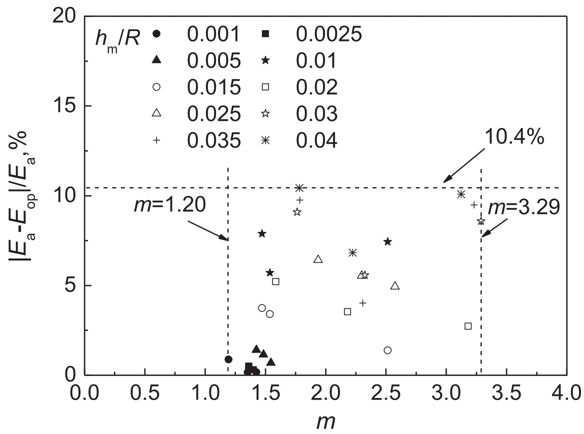

Fig. B2. Influence of the fitting parameter m on the error of the predicated elastic modulus by using the Oliver–Pharr method.

small (e.g., $h_m/R \le 0.01$), the error is less than 5%; the error increases rapidly with the normalized indentation depth h_m/R. If h_m/R remains constant, the error decreases with the increase in the percentage of the upper unloading data and it approaches a minimum value with the percentage of the upper unloading data in the range of 30–40%, and then sharply increases when the percentage of the upper unloading data is more than 40%. Therefore, it has been suggested that the upper 30–40% of the unloading data is used to fit the curve defined by Eq. (2b) in application of the Oliver–Pharr method for SMAs.

We also investigated the influence of the fitting parameter m on predicted elastic modulus, as shown in Fig. B2. It can be seen that when the percentage of the upper unloading data lies in the range of 30–40%, a reasonable range for the parameter m is between 1.20 and 3.29. At small indentation depths, e.g., $h_m/R \le 0.01$, m approaches 1.5, which is consistent with the range of 1.2–1.6 for most solid elasto-plastic materials with the Berkovich indenter (Oliver and Pharr, 1992). At large indentation depths, e.g.,$h_m/R > 0.01$, m can be larger than 2.0.

In conclusion, the contact stiffness S should be calculated by fitting the upper 30–40% of the unloading data and the fitted parameter m should be within the interval of 1.20–3.29.

References

Abaqus version 6.10-2, 2010. Dassault Systèmes Simulia Corp., Providence, RI, USA.

Amini, A., Yan, W., Sun, Q.P., 2011. Depth dependency of indentation hardness during solid-state phase transition of shape memory alloys. Appl. Phys. Lett. 021901, 99.

Auricchio, F., 1995. Shape-memory Alloys: Applications, Micromechanics, Macromodelling and Numerical Simulations (Ph.D. dissertation). Department of Civil Engineering, University of California at Berkeley.

Auricchio, F., Taylor, R.L., Lubliner, J., 1997. Shape-memory alloys: macromodelling and numerical simulations of superelastic behavior. Comput. Methods Appl. Mech. Eng. 46 (1), 281–312.

Auricchio, F., Taylor, R.L., 1997. Shape-memory alloys: modelling and numerical simulations of the finite-strain superelastic behavior. Comput. Methods Appl. Mech. Eng. 143 (1–2), 175–194.

Auricchio, F., Sacco, E., 1997a. A 1D model for superelastic shape memory alloys with different elastic properties between austenite and martensite. J. Non-linear Mech., 1101–1114.

Auricchio, F., Sacco, E., 1997b. A super-elastic shape-memory alloy beam model. J. Int. Mater. Syst. Struct., 1–13.

Buljak, V., Maier, G., 2012. Identification of residual stresses by instrumented elliptical indentation and inverse analysis. Mech. Res. Commun. 41, 21–29.

Cao, Y.P., Lu, J., 2005. Size-dependent sharp indentation—II: a reverse algorithm to identify plastic properties of metallic materials. J. Mech. Phys. Solids 53, 49–62.

Cheng, Y.T., Cheng, C.M., 1999. Scaling relationships in conical indentation of elastic–perfectly plastic solids. Int. J. Solids Struct. 36, 1231–1243.

Cheng, Y.T., Cheng, C.M., 2004. Scaling, dimensional analysis, and indentation measurements. Mater. Sci. Eng. R 44, 91–149.

Choi, I.S., Dao, M., Suresh, S., 2008. Mechanics of indentation of plastically graded materials—I: Analysis. J. Mech. Phys. Solids 56, 157–171.

Duerig, T., Pelton, A., Stöckel, D., 1999. An overview of nitinol medical applications. Mater. Sci. Eng. A 273-275, 149–160.

Dye, T.E., 1990. An Experimental Investigation of the Behavior of Nitinol (M.S. thesis). Virginia Polytechnic Institute and State University.

Ebenstein, D.M., Pruitt, L.A., 2006. Nanoindentation of biological materials. Nanotoday 1, 26–33.

Feng, P., Sun, Q.P., 2006. Experimental investigation on macroscopic domain formation and evolution in polycrystalline NiTi microtubing under mechanical force. J. Mech. Phys. Solids 54, 1568–1603.

Feng, X.Q., Qian, L.M., Yan, W., Sun, Q.P., 2008. Wearless scratch on NiTi shape memory alloy due to phase transformational shakedown. Appl. Phys. Lett. 92, 121909.

Fu, Y., Du, H., Huang, W., Zhang, S., Hu, M., 2004. TiNi-based thin films in MEMS applications: a review. Sens. Actuators A 112, 395–408.

Gall, K., Juntunen, K., Maier, H.J., Sehitoglu, H., Chumlyakov, Y.I., 2001. Instrumented micro-indentation of NiTi shape-memory alloys. Acta Mater. 49, 3205–3217.

Gao, H., Chiu, C.H., Lee, J., 1992. Elastic contact versus indentation modeling of multi-layered materials. Int. J. Solids Struct. 29, 2471–2492.

Giannakopoulos, A.E., Suresh, S., 1999. Determination of elastoplastic properties by instrumented sharp indentation. Scr. Mater. 40 (10), 1191–1198.

Hay, J.L., Pharr, G.M., 2000. ASM Handbook, Vol. 08. In: Kuhn, H., Medlin, D. (Eds.), . ASM International, Materials Park, OH, pp. 232–243.

Hertz, H., 1896. Miscellaneous Papers by H. Hertz. Macmillan, Lodon.

Holtz, R.L., Sadananda, K., Imam, M.A., 1999. Fatigue thresholds of Ni–Ti alloy near the shape memory transition temperature. Int. J. Fatigue 21, 137–145.

Humbeeck, J.V., 1999. Non-medical applications of shape memory alloys. Mater. Sci. Eng. A 273-275, 134–148.

Ishimoto, T., Nakano, T., Yamamoto, M., Tabata, Y., 2011. Biomechanical evaluation of regenerating long bone by nanoindentation. J. Mater. Sci. Mater. Med. 22, 969–976.
Jacobus, K., Sehitoglu, H., Balzer, M., 1996. Effect of stress state on the stress-induced martensitic transformation in polycrystalline Ni–Ti alloy. Metall. Mater. Trans. A 27A, 3067–3072.
Kang, G.Z., Yan, W., 2010. Scaling relationships in sharp conical indentation of shape memory alloys. Philos. Mag. 90 (5), 599–616.
Kang, G.Z., Kan, Q.H., Qian, L.M., Liu, Y.J., 2009. Ratchetting deformation of superelastic and shape memory NiTi alloys. Mech. Mater. 41 (2), 139–153.
King, R.B., 1987. Elastic analysis of some punch problems for a layered medium. Int. J. Solids Struct. 23, 1657–1664.
Li, Z.Q., Sun, Q.P., 2002. The initiation and growth of macroscopic martensite band in nano-grained NiTi microtube under tension. Int. J. Plasticity 18, 1481–1498.
Ni, W., Cheng, Y.T., Grummon, D.S., 2002. Recovery of microindents in a nickel–titanium shape-memory alloy: a "self-healing" effect. Appl. Phys. Lett. 80, 3310–3312.
Ni, W., Cheng, Y.T., Grummon, D.S., 2003. Microscopic superelastic behavior of a nickel–titanium alloy under complex loading conditions. Appl. Phys. Lett. 82, 2811–2813.
Nix, W.D., Gao, H., 1998. Indentation size effects in crystalline materials: a law for strain gradient plasticity. J. Mech. Phys. Solids 46, 411–425.
Oliver, W.C., Pharr, G.M., 1992. An improved technique for determining hardness and elastic modulus using load and displacement sensing indentation experiments. J. Mater. Res. 7, 1564–1583.
Oliver, W.C., Pharr, G.M., 2004. Measurement of hardness and elastic modulus by instrumented indentation: advances in understanding and refinements to methodology. J. Mater. Res. 19 (1), 3–20.
Oyen, M.L., Cook, R.F., 2009. A practical guide for analysis of nanoindentation data. J. Mech. Behav. Biomed. 2, 396–407.
Popov, P., Lagoudas, D.C., 2007. A 3-D constitutive model for shape memory alloys incorporating pseudoelasticity and detwinning of self-accommodated martensite. Int. J. Plasticity 23, 1697–1720.
Qian, L.M., Xiao, X.D., Sun, Q.P., Yu, T.X., 2004. Anomalus relationship between hardness and wear properties of a superelastic nickel–titanium alloy. Appl. Phys. Lett. 84, 1076–1078.
Qian, L.M., Sun, Q.P., Xiao, X.D., 2006. Role of Phase Transition in the unusual microwear behavior of superelastic NiTi shape memory alloy. Wear 260, 509–522.
Sun, Q.P., Li, Z.Q., 2002. Phase transformation in superelastic NiTi polycrystalline micro-tubes under tension and torsion-from localization to homogeneous deformation. Int. J. Solids Struct. 39, 3797–3809.
Wang, Y.M., Yue, Z.F., 2007. FEM prediction of the pseudoelastic behavior of NiTi SMA at different temperatures with one temperature testing results. Comput. Mater. Sci. 39 (3), 697–704.
Yan, W., Sun, Q.P., Feng, X.Q., Qian, L.M., 2006a. Determination of transformation stresses of shape memory alloy thin films: a method based on spherical indentation. Appl. Phys. Lett. 88, 241912.
Yan, W., Sun, Q.P., Liu, H.Y., 2006b. Spherical indentation hardness of shape memory alloys. Mater. Sci. Eng. A 425, 278–285.
Yan, W., Sun, Q.P., Feng, X.Q., Qian, L.M., 2007. Analysis of spherical indentation of super-elastic shape memory alloys. Int. J. Solids Struct. 44, 1–17.
Yan, W., Sun, Q.P., L, H. Y, 2008. Effect of transformation volume strain on the spherical indentation of shape memory alloys. Int. J. Mod. Phys. B 22 (31&32), 5957–5964.
Zaki, W., Moumni, Z., 2007. A 3-D model of the cyclic thermomechanical behavior of shape memory alloys. J. Mech. Phys. Solids 55, 2427–2454.
Zhang, L., Xie, C.Y., Wu, J.S., 2006. Progress in research on shape memory alloy films in MEMS field. Mater. Rev. 2, 109–113.
Zhao, M., Chen, X., Yan, J., Karlsson, A.M., 2006. Determination of uniaxial residual stress and mechanical properties by instrumented indentation. Acta Mater. 54, 2823–2832.
Zysset, P.K., Guo, X.E., Hoffler, C.E., Moore, K.E., Goldstein, S.A., 1999. Elastic modulus and hardness of cortical and trabecular bone lamellae measured by nanoindentation in the human femur. J. Biomech. 32, 1005–1012.